2D Materials

Quantum confinement and photoresponsivity of β-In_2Se_3 nanosheets grown by physical vapour transport

To cite this article: Nilanthy Balakrishnan *et al* 2016 *2D Mater.* **3** 025030

2D Materials

OPEN ACCESS

RECEIVED
4 February 2016

REVISED
21 April 2016

ACCEPTED FOR PUBLICATION
29 April 2016

PUBLISHED
3 June 2016

PAPER

Quantum confinement and photoresponsivity of β-In_2Se_3 nanosheets grown by physical vapour transport

Nilanthy Balakrishnan[1], **Christopher R Staddon**[1], **Emily F Smith**[2], **Jakub Stec**[1], **Dean Gay**[1], **Garry W Mudd**[1], **Oleg Makarovsky**[1], **Zakhar R Kudrynskyi**[1], **Zakhar D Kovalyuk**[3], **Laurence Eaves**[1], **Amalia Patanè**[1] and **Peter H Beton**[1]

[1] School of Physics and Astronomy, University of Nottingham, Nottingham NG7 2RD, UK
[2] School of Chemistry, University of Nottingham, Nottingham, NG7 2RD, UK
[3] Institute for Problems of Materials Science, The National Academy of Sciences of Ukraine Chernivtsi, 58001, Ukraine

E-mail: peter.beton@nottingham.ac.uk, nilanthy.balakrishnan@nottingham.ac.uk and amalia.patane@nottingham.ac.uk

Keywords: indium selenide, quantum confinement, photodetector, III–VI semiconductor, physical vapour deposition

Supplementary material for this article is available online

Abstract

We demonstrate that β-In_2Se_3 layers with thickness ranging from 2.8 to 100 nm can be grown on SiO_2/Si, mica and graphite using a physical vapour transport method. The β-In_2Se_3 layers are chemically stable at room temperature and exhibit a blue-shift of the photoluminescence emission when the layer thickness is reduced, due to strong quantum confinement of carriers by the physical boundaries of the material. The layers are characterised using Raman spectroscopy and x-ray diffraction from which we confirm lattice constants $c = 28.31 \pm 0.05$ Å and $a = 3.99 \pm 0.02$ Å. In addition, these layers show high photoresponsivity of up to $\sim 2 \times 10^3$ A W^{-1} at $\lambda = 633$ nm, with rise and decay times of $\tau_r = 0.6$ ms and $\tau_d = 2.5$ ms, respectively, confirming the potential of the as-grown layers for high sensitivity photodetectors.

1. Introduction

The integration of layered semiconductors with graphene to form heterostructure devices offers new routes to the fabrication of optoelectronic devices such as fast, ultrasensitive photodetectors [1–3]. Metal dichalcogenides (MoS_2 and WSe_2), III–VI semiconductors (InSe, GaSe and In_2Se_3), and elemental semiconductors (black phosphorus), are currently being studied as potential candidate materials for these applications [1–9]. The III–VI materials exhibit an interesting dependence of the bandgap on the layer thickness which has been identified for exfoliated flakes of InSe, GaSe, and GaTe, and has been attributed to the formation of a two-dimensional quantum well with potential barriers formed by the physical boundaries of the exfoliated flakes [10–12]. This effect offers the prospect of band-gap engineering in the III–VI system through the tailoring of layer thickness to control optoelectronic properties, notably the absorption edge and photoluminescence energy of emitted photons. Quantum confinement has so far been demonstrated clearly only for exfoliated crystals and has not been reported to date for thin films grown on a substrate. This raises questions as to whether thin film growth techniques provide material and interfaces of sufficient quality for the observation of such quantum effects.

In this paper we demonstrate quantum confinement in the In_2Se_3 material system, both for exfoliated flakes, and for thin films grown by physical vapour transport. Among the III–VI crystals, In_2Se_3 can occur as several different crystal structures and phases (α, β, γ, δ, and κ) [13, 14]. The α- and β-In_2Se_3 are van der Waals layered crystals and have attracted particular interest. For both phases, the primitive unit cell contains three layers, each consisting of five closely-packed, covalently bonded, monoatomic sheets in the sequence Se–In–Se–In–Se (figure 1(a)). As proposed in [15], in α-In_2Se_3 the outer Se-atoms in each layer are aligned, whereas in β-In_2Se_3 they are located in the interstitial sites of the Se-atoms in the neighbouring layers, thus leading to a smaller volume in β-In_2Se_3, but without changing the crystal symmetry [15].

The growth of thin films of α-In_2Se_3 with excellent structural properties has been reported recently [8, 16, 17], but the growth of two-dimensional β-In_2Se_3 remains largely unexplored although this phase exhibits significant differences in its electrical properties, including a stronger sensitivity of the electronic band structure to externally applied electric fields [18, 19].

As we show below β-In_2Se_3 layers can be grown on several different substrates (SiO_2/Si, mica and graphite) and quantum confinement can indeed be realized for thin films grown on SiO_2/Si. Specifically, using γ-InSe as source material we demonstrate the growth of β-In_2Se_3 islands with typical widths 1–15 μm and thickness ranging from 100s of nanometers down to 2.8 nm. The presence of β-In_2Se_3 is confirmed using a combination of Raman spectroscopy, x-ray diffraction (XRD), elemental analysis and photoluminescence. Our results are unexpected since there have been several other studies which have found that a different phase, α-In_2Se_3, is commonly observed under somewhat similar growth conditions [8, 16, 17]. In addition, the stability of β-In_2Se_3 has been questioned and some interconversion between different phases has been reported [14, 18, 20]. However, we found that our grown films display excellent stability under a long period of storage in ambient conditions. Moreover, we observe a shift in the photoluminescence peak due to quantum confinement which is controlled by the physical thickness of the β-In_2Se_3 islands; this indicates that the effects previously reported for exfoliated layers can also be realized in films grown on a substrate, offering the prospect of band-gap engineering in large-area devices. Furthermore, our work implies that a high quality heterojunction is formed between the substrate and the β-In_2Se_3 island since this interface provides one of the barriers which leads to carrier confinement. The grown material may be readily incorporated into simple devices for high sensitivity photodetection.

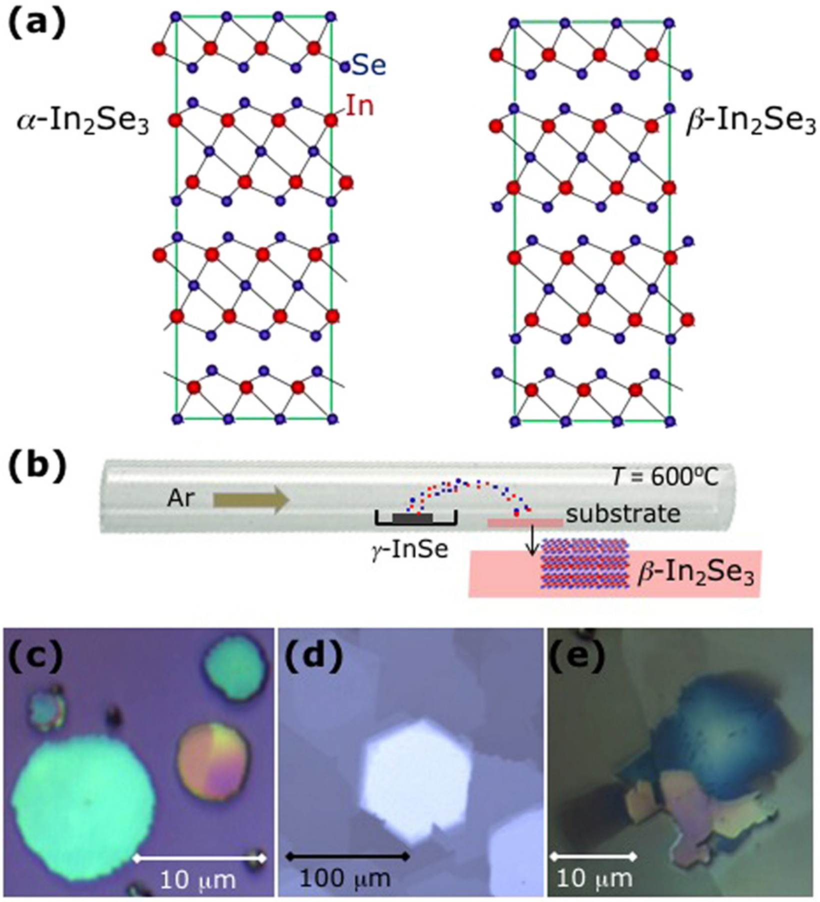

Figure 1. Growth of β-In_2Se_3 layers and their optical micrographs: (a) side view of the crystal lattice and unite cell of α-In_2Se_3 (left) and β-In_2Se_3 (right) following [15]. Blue and red spheres correspond to Se- and In-atoms, respectively. (b) Schematic diagram of a tube furnace used for the growth of In_2Se_3 layers. γ-InSe powder is used as source material. (c)–(e) Optical micrographs of β-In_2Se_3 layers grown on SiO_2/Si, mica, and graphite, respectively.

2. Methods

2.1. Synthesis of In_2Se_3 layers

A Bridgman-grown γ-InSe ingot [21] was ground into powder and placed at the centre of a tube furnace. An Ar flow of 150 sccm provided a pressure of 1.6 mbar and carried the vapour to deposit on the substrate, placed downstream about 6–10 cm away from the source material. The γ-InSe powder was heated to $T = 590$ °C (mica) or 600 °C (SiO_2, graphite) for 12 h prior to the growth of the In_2Se_3 layers. The system was then allowed to cool back to room temperature (RT).

2.2. Characterisation

Images of the In_2Se_3 layer topography were acquired by AFM in tapping mode under ambient conditions. The XRD data were obtained with a PANalytical X'Pert Materials Research Diffractometer, using two different configurations for the lattice constant determination along the *c*-axis and the in-plane hexagonal axes. For the *c*-axis parameter measurement, a line focus was used with an x-ray mirror and an asymmetric monochromator with a Cu-$K_{\alpha 1}$ wavelengths of $\lambda K_{\alpha 1} = 1.540\,56$ Å and a PIXCEL detector with a 1° receiving slit. For in-plane diffraction, a point focus and primary x-ray lens was used with non-monochromator and a detector with a parallel plate collimator and flat plate monochromator to exclude Cu-Kβ radiation. Hence the wavelength used for this measurement is $\lambda K_{\alpha 1}/K_{\alpha 2} = 1.5418$ Å. The lattice constant along the *c*-axis and the hexagonal axes were determined, respectively, from (00*l*) reflections and $(\bar{1}20)$ and $(1\bar{2}0)$ reflections. The XPS measurements were carried out using a Kratos AXIS ULTRA with a monochromatic Al Kα x-ray source ($h\nu = 1486.6$ eV) operated at 10 mA emission current and 12 kV anode potential ($P = 120$ W), and the data processing was carried out using CASAXPS software with Kratos sensitivity factors (RSFs) to determine atomic % values from the peak areas. All XPS binding energies were calibrated with respect to the C 1s peak at a binding energy of 284.8 eV.

The experimental set-up for Raman and μPL measurements comprised a He–Ne laser ($\lambda = 633$ nm) and a frequency-doubled Nd:YVO_4 laser ($\lambda = 532$ nm), an XY linear positioning stage or a cold finger cryostat, an optical confocal microscope system, a spectrometer with 150 and 1200 groves mm^{-1} gratings, equipped with a charge-coupled device and a liquid-nitrogen cooled (InGa)As array photodetector. The laser beam was focused to a diameter $d \approx 1\ \mu$m using a 100× objective and the Raman and μPL spectra were measured at low power ($P \leqslant 0.3$ mW) to avoid lattice heating. For the measurement of the photocurrent spectra, light from a 250 W quartz halogen lamp was dispersed through a 0.25 m monochromator (bandwidth of ≈10 nm). Light was modulated with a mechanical chopper (frequency $f = 22$ Hz) and focused onto the device ($P \approx 10^{-3}$ W cm^{-2}). The photocurrent signal was measured using a Stanford SR830 lock-in amplifier (integration time constant of $t = 10$ s).

The measurements of the DC dark current and photocurrent versus the applied voltage were acquired using a Keithley 2400 source-meter. The temporal dynamics of the photocurrent was investigated under constant bias voltage ($V = 1$ V) and illumination by a mechanically modulated He–Ne laser with $\lambda = 633$ nm, $P \approx 17$ nW and frequency f in the range of 1–500 Hz. The photocurrent signal was measured using a Tektronix DPO 4032 digital oscilloscope and a Keithley 2400 was used as a DC voltage source. The device was connected in series with a 1 MΩ resistor. We measured the voltage drop across the resistor, which enabled us to measure voltage signals with a low noise level.

3. Results and discussion

The β-In_2Se_3 layers were grown by a physical vapour transport method, as illustrated in figure 1(b). A ground powder of Bridgman-grown γ-InSe crystals was used as source material [21]. We found that growth on SiO_2/Si substrates produces near-circular, slightly facetted films with lateral size between 1 and 15 μm (figure 1(c)), while highly facetted hexagonal films with lateral size ~100 μm grew on mica under similar conditions, see figure 1(d). On graphite, films with arbitrary shape grew (figure 1(e)) with preferential growth at step edge bunches on the substrate. Figure 2 shows optical micrographs (figure 2(a)), topographic atomic force microscopy (AFM) images (figure 2(b)) and corresponding height profiles (bottom of figure 2(b)) of typical films grown on a SiO_2/Si substrate. The thickness L of the In_2Se_3 layers was determined by AFM. The thinnest measured films have a thickness of $L \approx 2.8$ nm, which corresponds to the size of a unit cell along the *c*-axis for β-In_2Se_3 (see figure 3(b)). Additionally, single monolayer steps (≈1 nm) were observed on the surface of some of the investigated films.

Identifying the crystalline phase of the as-grown In_2Se_3 layers has proven challenging due to multiple phases (α, β, γ, δ, and κ) existing at different temperatures [13, 14]. While the crystal structures of γ- and δ-In_2Se_3 are hexagonal and trigonal, respectively [22], the rhombohedral crystal structures of α- and β-In_2Se_3 phases are quite similar and different symmetries (with space group R3m and R$\bar{3}$m) have been suggested by some reports [19, 22, 23], while others have argued that the two phases have the same symmetry [15]. In previous studies of bulk In_2Se_3 it has been shown that the α-phase, which is stable at RT, reversibly transforms into the β-phase at $T = 200$ °C by thermal annealing [14, 23]. However, a recent report has shown that the β-phase can persist in thin layers

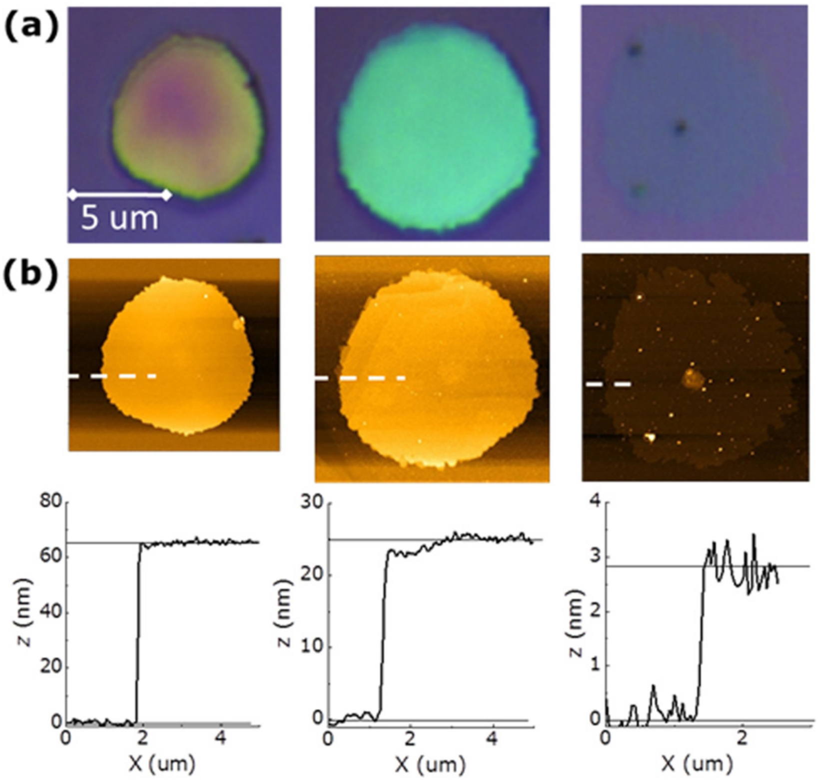

Figure 2. Topographical characterisation of In_2Se_3 layers: (a) optical micrographs and (b) topographic AFM images and z-profiles (bottom) of In_2Se_3 layers grown on a SiO_2/Si substrate. The AFM z-profiles were obtained along the dashed lines shown in the AFM images. The thinnest film grown on SiO_2/Si substrate has layer thickness of ~2.8 nm.

(~4–5 nm) at RT [18]. To discriminate between different phases in our experiments we use a combination of Raman spectroscopy and XRD.

RT (T = 300 K) micro-Raman spectra of representative films grown on SiO_2/Si substrate are shown in figure 3(a). The Raman peaks are centred at ~110, 175, and 205 cm^{-1} and correspond to the phonon modes of β-In_2Se_3 [15, 18, 20, 24]. The main Raman line at ~110 cm^{-1} corresponds to the A_1(LO+TO) phonon mode and the weaker peaks at ~175 and 205 cm^{-1} are attributed to the A_1(TO) mode and A_1(LO) mode, respectively. In comparison, the A_1(LO+TO), A_1(TO), and A_1(LO) phonon modes in exfoliated flakes of α-In_2Se_3 crystals [24] grown by the Bridgman method are at ~104, 181, and 200 cm^{-1}, respectively [15, 18, 20, 24], see bottom of figure 3(a) (further details can be found in supporting information figure S1). Therefore, our Raman spectra indicate that the grown layers are β-In_2Se_3 and that they are stable at RT consistent with a recent report [18].

The inset of figure 3(a) shows the Raman shift versus layer thickness of the A_1(LO+TO), A_1(TO), and A_1(LO) peaks of as-grown β-In_2Se_3. The A_1(LO+TO) mode at ~110 cm^{-1} does not depend on the layer thickness, although, the A_1(TO), and A_1(LO) phonon modes exhibit a small shift to lower wavenumbers with decreasing L. This could arise from the smaller vibration coherence length along the c-axis due to the weak van der Waals force along this direction [26]. When the layer thickness L decreases below ~10 nm, the full width at half maximum (W) of the 110 cm^{-1} Raman line tends to broaden by a factor of ~1.4, possibly due to the roughness of the film and its interface with the SiO_2 substrate [27].

XRD and x-ray photoelectron spectroscopy (XPS) measurements are also consistent with the formation of the β-In_2Se_3 phase (figures 1(a) and 3(b)). Within each plane, atoms form hexagons with lattice parameter a = 4.00 Å; along the c-axis, the lattice parameter is c = 28.33 Å [22, 23]. The equivalent lattice parameters for α-In_2Se_3 are a = 4.025 Å and c = 28.762 Å [22, 23]. Figure 3(c) shows a typical XRD spectrum of as-grown films on a SiO_2/Si substrate at T = 300 K which confirms that the In_2Se_3 layers are highly crystalline with a lattice constant along the c-axis, $c = 28.31 \pm 0.05$ Å, and along the hexagonal axes, $a = 3.99 \pm 0.02$ Å (see supporting information figure S2 which shows the XRD measurements of the $(\bar{1}20)$ and $(1\bar{2}0)$ reflections from which the value for a is derived). Our XRD values of the lattice constants (a and c) are in excellent agreement with the reported values of β-In_2Se_3 in [22, 23] and rule out the presence of α-In_2Se_3. Additionally, our XPS spectra show that the stoichiometric composition of the layers is $[In] \approx 42 \pm 3$ atomic % and $[Se] \approx 58 \pm 3$ atomic %, close to [In]:[Se] ≈ 2:3, see supporting information figure S3.

Room temperature (T = 300 K) μPL spectra of representative films grown on SiO_2/Si substrate are

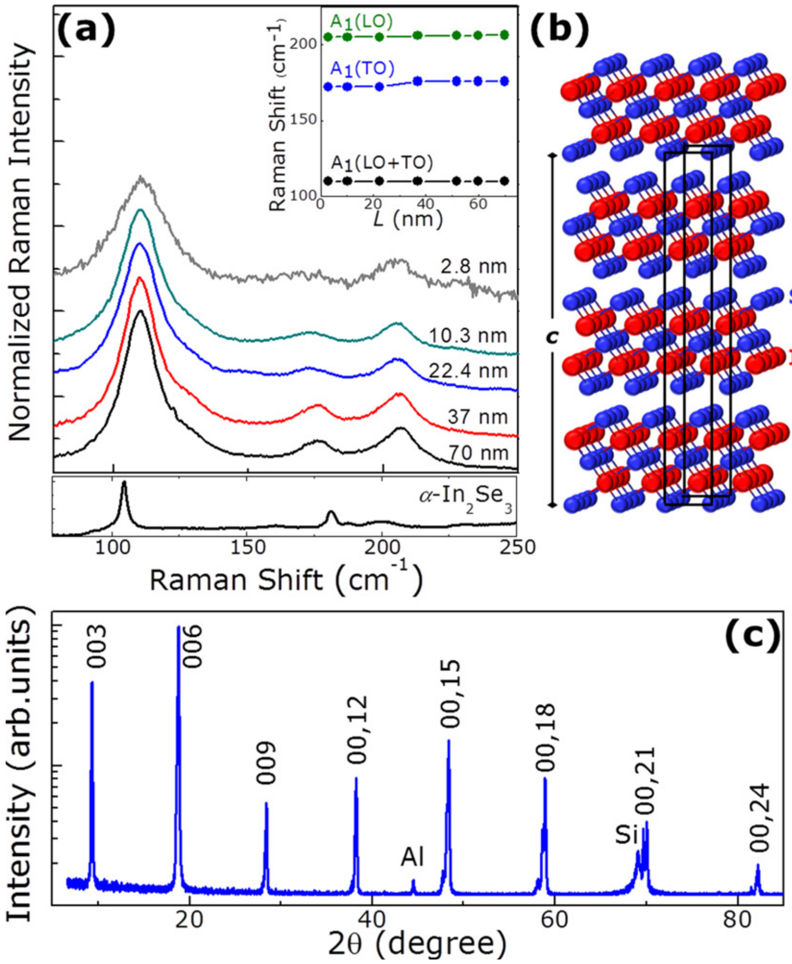

Figure 3. Characterisation of the crystal structure of In_2Se_3 layers: (a) normalised Raman spectra of β-In_2Se_3 layers (top) and exfoliated Bridgman-grown α-In_2Se_3 (bottom) at $T = 300$ K ($P = 0.1$ mW and $\lambda = 633$ nm). The main Raman mode at ~110 cm^{-1} corresponds to the A_1(LO + TO) phonon mode of β-In_2Se_3. The weaker peaks at ~175 and 205 cm^{-1} are attributed to the A_1(TO) and A_1(LO) phonon modes of β-In_2Se_3, respectively. The inset shows the Raman shift versus layer thickness of the A_1(LO + TO), A_1(TO) and A_1(LO) peaks. (b) Schematic crystal structure of rhombohedral β-In_2Se_3, which belongs to the $R\bar{3}m$ space group. (c) Typical XRD spectra of β-In_2Se_3 at $T = 300$ K and ambient conditions. The low intensity peak at ~44.4° corresponds to Al from the sample holder.

shown in figure 4(a). The PL peak occurs at a photon energy $h\nu = 1.43$ eV for films with $L > 50$ nm. With decreasing L, the PL emission exhibits a blue-shift by up to 160 meV (figures 4(a) and (b)), consistent with quantum confinement of photo-excited carriers by the external surfaces of the films. In addition, when L decreases below ~30 nm, the PL intensity decreases by a factor of two or more partly due to the weaker absorption of light ($\alpha \approx 1 \times 10^7$ m^{-1} at $\lambda = 532$ nm [28], where α is the absorption coefficient of In_2Se_3) and the full width at half maximum (W) of the PL emission increases by a factor of two possibly due to the roughness of the layers and/or crystal defects. The PL emission of these films persists for several months when they are stored under ambient conditions, confirming their chemical stability. No PL signal was detected at $T = 300$ K from the thinnest In_2Se_3 films ($L = 2.8$ nm) identified by AFM.

Figure 4(b) shows the results of PL and AFM measurements of several as-grown β-In_2Se_3 layers (black dots) and our exfoliated Bridgman-grown α-In_2Se_3 [25] flakes (blue stars) on the SiO_2/Si substrate. They reveal the dependence of the band-to-band transition energy, E_{2D}, on the layer thickness L. RT PL spectra of representative exfoliated α-In_2Se_3 flakes are shown in the supporting information figure S4. Figure 4(b) also shows the RT PL peak energy of α-In_2Se_3 thin layers (red stars) grown by physical vapour transport as reported in [17].

We model the dependence of E_{2D} on L using a square quantum well potential of infinite height, i.e.

$$E_{2D} = E_g - E_b + \pi^2\hbar^2/2L^2\mu_{\parallel c}, \tag{1}$$

where E_g is the optical band gap energy at $T = 300$ K, E_b is the exciton binding energy, $\mu_{\parallel c} = \left(\frac{1}{m^e_{\parallel c}} + \frac{1}{m^h_{\parallel c}}\right)^{-1}$ is the exciton reduced mass for motion along the c-axis in In_2Se_3. The values of $E_g - E_b$ and $\mu_{\parallel c}$ are obtained from the best fit to the measured values of the PL peak energy (at $T = 300$ K) versus layer thickness. The value of the exciton reduced mass along the c-axis of bulk β-In_2Se_3, $\mu_{\parallel c} = 0.030\, m_e$, is smaller than the value for α-

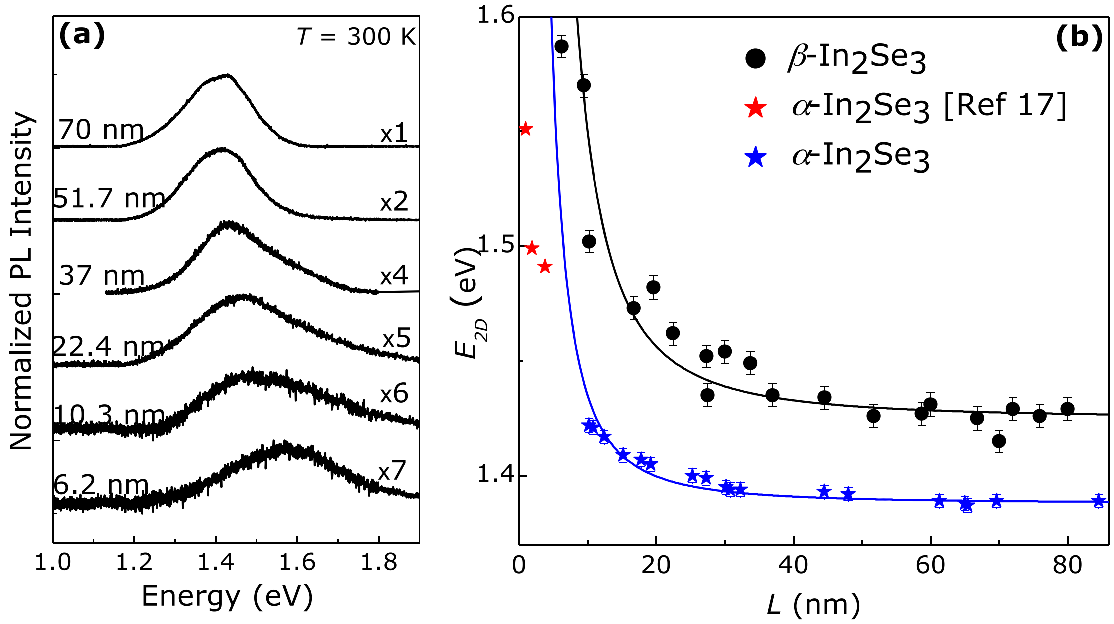

Figure 4. PL spectra and quantum confinement effect: (a) normalised μPL spectra of β-In$_2$Se$_3$ layers at $T = 300$ K ($P = 0.3$ mW and $\lambda = 532$ nm). (b) Measured dependence of the peak energy, E_{2D}, of the μPL emission at $T = 300$ K on the layer thickness L of the as-grown β-In$_2$Se$_3$ (black dots), exfoliated Bridgman-grown α-In$_2$Se$_3$ flakes (blue stars) and α-In$_2$Se$_3$ thin layers grown by the physical vapour transport method (red stars) [17]. The continuous lines show the calculated dependence of the exciton recombination energy for an infinite height quantum well of width L at $T = 300$ K.

In$_2$Se$_3$ ($\mu_{\parallel c} = 0.080\ m_e$) and for γ-InSe ($\mu_{\parallel c} = 0.054\ m_e$) [10]; here m_e is the electron mass in vacuum. This indicates a stronger quantum confinement effect in β-In$_2$Se$_3$ compared to α-In$_2$Se$_3$ and γ-InSe. The scatter in the individual data points around the modelled curves (continuous lines) suggest that carrier confinement is influenced by the roughness of the layers and its interface with the substrate and/or crystal defects. In recent theoretical work it has been argued that bulk β-In$_2$Se$_3$ has an indirect band gap and remains indirect when the layer thickness is reduced to a single layer with a shift of the bandgap energy by 590 meV [19]. Our experimental data are in qualitative agreement with this theoretical study. However, the higher energy PL peak position for bulk β-In$_2$Se$_3$ compared to α-In$_2$Se$_3$ is opposite to that predicted in [19] and requires further investigation and modelling of the crystal structure for different atomic arrangements. RT PL emission has also been detected from our β-In$_2$Se$_3$ films (with $L > 50$ nm) grown on mica and graphite, shown in the supporting information figures S5 and S6, respectively.

In order to study the photoconductivity of the as-grown β-In$_2$Se$_3$ layers, we have fabricated photodetectors based on representative films with thickness down to $L = 20$ nm. For the electrodes, Ti/Au (10 and 100 nm, respectively) contacts were deposited using a combination of evaporation and electron beam lithography. The photocurrent spectra indicate a systematic blue-shift of the absorption edge with decreasing layer thickness and do not show a clear excitonic absorption band, suggesting that the β-In$_2$Se$_3$ has an indirect band gap, as predicted in [19], see figure 5.

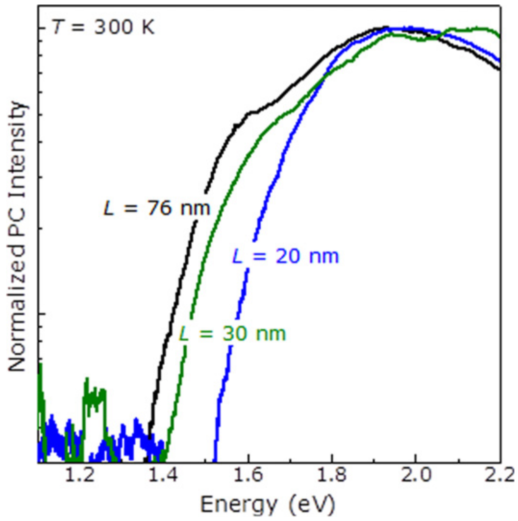

Figure 5. Photoconductivity spectra of two-terminal Au/In$_2$Se$_3$ devices at $V = 1$ V and $T = 300$ K ($P = 10^{-3}$ W cm^{-2}). The spectra for the β-In$_2$Se$_3$ layers with $L = 20$ nm (blue) and $L = 30$ nm (green) are blue-shifted to higher energy relative to the film with $L = 76$ nm (black).

Figure 6(a) shows the current–voltage, I–V, characteristics of a β-In$_2$Se$_3$ photodetector ($L = 76$ nm) measured under dark and illuminated conditions ($\lambda = 633$ nm, $P = 170\ \mu$W) at $T = 300$ K. Under illumination by a focused laser beam, the current increases, particularly for $V > 0.5$ V. The dependence of the photocurrent, ΔI, on the applied bias under different laser powers is shown in figure 6(b). A spatially resolved photocurrent map obtained by scanning a

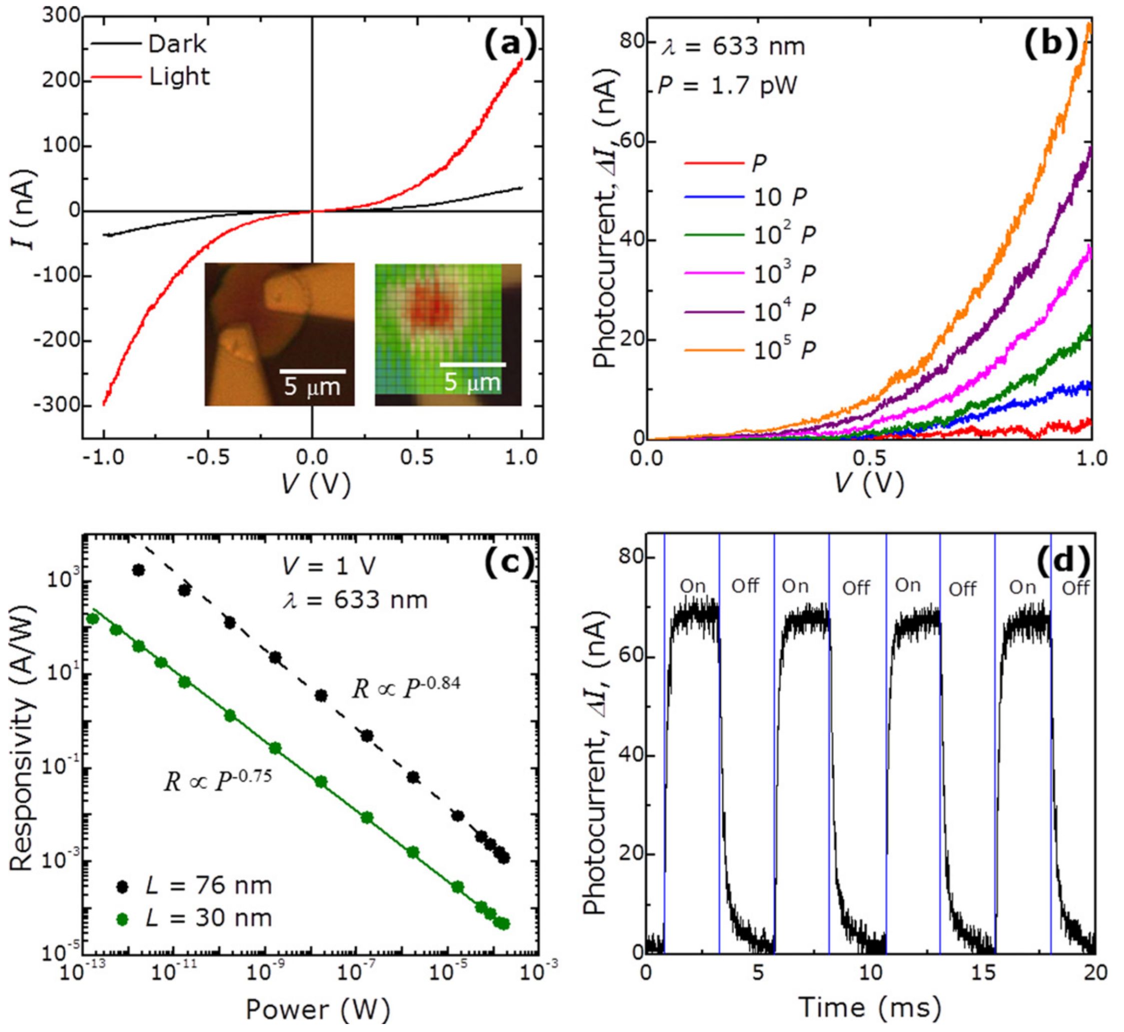

Figure 6. Photoconductive response of β-In_2Se_3 layers: (a) current–voltage, I–V, characteristics measured under dark and illuminated ($\lambda = 633$ nm, $P = 170\ \mu$W) conditions for a single In_2Se_3 film with thickness $L \sim 76$ nm ($T = 300$ K). The insets show the optical image (left) and a photocurrent map (right) of the device. (b) Photocurrent, ΔI, versus applied bias, V, at $T = 300$ K for the device shown in (a). The photocurrent is measured with a focused laser beam of power in the range from P to 10^5P ($P = 1.7$ pW, $\lambda = 633$ nm, $T = 300$ K). (c) Photoresponsivity versus laser power at $T = 300$ K, $\lambda = 633$ nm, and $V = 1$ V for devices with layer thickness $L \sim$ 76 nm (black) and 30 nm (green). The dashed lines are fits to the data by an empirical power law, $R \propto P^{-n}$. (d) Temporal dependence of the photocurrent ($V = 1$ V, $\lambda = 633$ nm and $P = 17$ nW) of the device with layer thickness $L \sim 76$ nm.

focused laser beam ($\lambda = 633$ nm and $P = 17$ nW) across the plane of the In_2Se_3 layer shows that photocurrent generation occurs primarily in the In_2Se_3 region of the film between the two Ti/Au electrodes (see inset of figure 6(a)).

Under an applied bias V, photo-excited electrons and holes in In_2Se_3 are swept by the electric field in opposite directions, thus generating a photocurrent $\Delta I = [eL\alpha P/h\nu](\tau_l/\tau_t)$, where α is the absorption coefficient of In_2Se_3 at the photon energy $h\nu$, P is the incident power, e is the electronic charge, and τ_l/τ_t is the ratio of the carrier lifetime (τ_l) and transit time (τ_t) of electrons in In_2Se_3 [5]. Thus the photoresponsivity R of our device can be described approximately by the relation $R = \Delta I/P = [eL\alpha\tau_l/h\nu\tau_t]$. Moreover, we can express the external and internal quantum efficiencies as $\mathrm{EQE} = Rh\nu/e = L\alpha\tau_l/\tau_t$ and $\mathrm{IQE} = \tau_l/\tau_t$, respectively.

The In_2Se_3 photodetectors exhibit a stable and reproducible photoresponsivity, $R = \Delta I/P$, (figure 6(c)) with values of R of up to ~1720 A W^{-1} at $V = 1$ V, $\lambda = 633$ nm and low incident power $P = 1.7$ pW, which corresponds to an $\mathrm{IQE} = \tau_l/\tau_t \approx 5.5 \times 10^3$ for $\alpha \approx 8 \times 10^6\ \mathrm{m^{-1}}$ at $h\nu = 1.96$ eV ($\lambda = 633$ nm) [28] and $L = 76$ nm. From the maximum value of R (for $L = 76$ nm), we estimate an external quantum efficiency EQE ≈ 3370 and a specific detectivity $D^* = R(A/2eI)^{1/2} \approx 7 \times 10^{10}\ \mathrm{m\ W^{-1}\ s^{-1/2}}$, where $A \approx 20\ \mu\mathrm{m}^2$ is the area of the film and $I = 36$ nA is the dark current at $V = 1$ V. A power law relation of the form $R \propto P^{-n}$ provides a good empirical fit to the values of R versus P for devices with $L = 30$ and 76 nm, with $n = 0.75$ and 0.84, respectively.

The photodetector response time was measured by focusing a mechanically modulated laser beam of $\lambda = 633$ nm and $P = 17$ nW on the device ($L = 76$ nm).

Figure 6(d) shows the photocurrent waveform in response to a series of cycles with the laser beam alternately on and off. Our In_2Se_3 photodetector exhibits a repeatable and stable response to the incident light. The measured rise (τ_r) and decay (τ_d) times are 0.6 and 2.5 ms, respectively. Our values of R and the rise/decay times for photodetectors based on as-grown nanosheets are comparable or superior to those reported previously for α-In_2Se_3 [29–31]. The direct growth of β-In_2Se_3 nanosheets on different substrates also offers flexibility for 2D electronic and optoelectronics.

4. Conclusions

In summary, we have grown β-In_2Se_3 layers by a physical vapour transport method. The β-In_2Se_3 layers are chemically stable and optically active at RT over periods of several months. Due to the smaller exciton mass along the c-axis, the 2D quantum confinement effects which we observe in β-In_2Se_3 are stronger than those previously reported in other III–VI van der Waals crystals, e.g., GaSe and GaTe [11, 12]. The thickness of the film can be used to tune the absorption and emission in the technologically relevant-midinfrared spectral range between 1.43 and 1.58 eV. The β-In_2Se_3 photodetectors showed excellent photoresponsivity and relatively fast response to light. These properties confirm that the β-In_2Se_3 layers are promising candidate materials for optoelectronic applications.

Acknowledgments

This work was supported by the Engineering and Physical Sciences Research Council (EPSRC) [under grants EP/M012700/1 and EP/K005138/1], the EU FP7 Graphene Flagship Project 604391, the University of Nottingham, and the Ukrainian Academy of Sciences.

References

[1] Zhang W *et al* 2014 *Sci. Rep.* **4** 3826

[2] Roy K, Padmanabhan M, Goswami S, Sai T P, Kaushal S and Ghosh A 2013 *Solid State Commun.* **175–176** 35–42

[3] Tielrooij K J *et al* 2015 *Nat. Nanotechnol.* **10** 437–43

[4] Georgiou T *et al* 2012 *Nat. Nanotechnol.* **8** 100–3

[5] Mudd G W *et al* 2015 *Adv. Mater.* **27** 3760–6

[6] Chen Z, Biscaras J and Shukla A 2015 *Nanoscale* **7** 5981–6

[7] Li X *et al* 2015 *ACS Nano* **9** 8078–88

[8] Lin M *et al* 2013 *J. Am. Chem. Soc.* **135** 13274–7

[9] Avsar A, Vera-Marun I J, Tan J Y, Watanabe K, Taniguchi T, Castro Neto A H and Özyilmax B 2015 *ACS Nano* **9** 4138–45

[10] Mudd G W *et al* 2013 *Adv. Mater.* **25** 5714–8

[11] Hu P, Wen Z, Wang L, Tan P and Xiao K 2012 *ACS Nano* **6** 5988–94

[12] Hu P *et al* 2014 *Nano Res.* **7** 694–703

[13] Jasinski J, Swider W, Washburn J, Liliental-Weber Z, Chaiken A, Nauka K, Gibson G A and Yang C C 2002 *Appl. Phys. Lett.* **81** 4356–8

[14] Julien C, Chevy A and Siapkas D 1990 *Phys. Status Solidi* **118** 553–9

[15] Feng K *et al* 2014 *Appl. Phys. Lett.* **104** 212102

[16] Li Q-L, Liu C-H, Nie Y-T, Chen W-H, Gao X, Sun X-H and Wang S-D 2014 *Nanoscale* **6** 14538–42

[17] Zhou J, Zeng Q, Lv D, Sun L, Niu L, Fu W, Liu F, Shen Z, Jin C and Liu Z 2015 *Nano Lett.* **15** 6400–5

[18] Tao X and Gu Y 2013 *Nano Lett.* **13** 3501–5

[19] Debbichi L, Eriksson O and Lebègue S 2015 *J. Phys. Chem. Lett.* **6** 3098–103

[20] Rasmussen A M, Teklemichael S T, Mafi E, Gu Y and McCluskey M D 2013 *Appl. Phys. Lett.* **102** 062105

[21] Kovalyuk Z D, Sydor O M, Sydor O A, Tkachenko V G, Maksymchuk I M, Dubinko V I and Ostapchuk P M 2012 *J. Mater. Sci. Eng.* A **2** 537–43

[22] Han G, Chen Z G, Drennan J and Zou J 2014 *Small* **10** 2747–65

[23] Popović S, Tonejc A, Gržeta-Plenković B, Čelustka B and Trojko R 1979 *J. Appl. Crystallogr.* **12** 416–20

[24] Lewandowska R, Bacewicz R, Filipowicz J and Paszkowicz W 2001 *Mater. Res. Bull.* **36** 2577–83

[25] Bakhtinov A P, Boledzyuk V B, Kovalyuk Z D, Kudrynskyi Z R, Lytvyn O S and Shevchenko A D 2013 *Phys. Solid State* **55** 1148–55

[26] Schwarcz R, Kanehisa A, Jouanne M, Morhange F and Eddrief M 2002 *J. Phys.: Condens. Matter* **14** 967–73

[27] Patanè A, Polimeni A and Capizzi M 1995 *Phys. Rev.* B **52** 2784–8

[28] Ei-Shair H T and Bekheet A E 1992 *J. Phys. D: Appl. Phys.* **25** 1122–30

[29] Jacobs-Gedrim R B, Shanmugam M, Jain N, Durcan C A, Murphy M T, Murray T M, Matyi R J, Moore R L II and Yu B 2014 *ACS Nano* **8** 514–21

[30] Island J O, Blanter S I, Buscema M, van der Zant H S J and Castellanos-Gomez A 2015 *Nano Lett.* **15** 7853—7858

[31] Buscema M, Island J O, Groenendijk D J, Blanter S I, Steele G A, van der Zant H S and Castellanos-Gomez A 2015 *Chem. Soc. Rev.* **44** 3691–718